Journal of Alloys and Compounds 512 (2012) 39–46

Contents lists available at SciVerse ScienceDirect

Journal of Alloys and Compounds

journal homepage: www.elsevier.com/locate/jallcom

Hot deformation behavior of Co-base ODS alloys

Lin Zhang[a,b], Xuanhui Qu[a,*], Xinbo He[a], Rafi-ud Din[a], Mingli Qin[a], Hongmin Zhu[b]

[a] State Key Laboratory for Advanced Metals and Materials, Beijing Key Laboratory for Powder Metallurgy and Particulate Materials, University of Science and Technology Beijing, Beijing 100083, PR China
[b] School of Metallurgical and Ecological Engineering, University of Science and Technology Beijing, Beijing 100083, PR China

ARTICLE INFO

Article history:
Received 13 July 2011
Received in revised form 26 August 2011
Accepted 30 August 2011
Available online 21 September 2011

Keywords:
High-temperature alloys
Mechanical alloying
Mechanical properties
Scanning electron microscopy

ABSTRACT

Co-base ODS alloys, strengthened by nanosized oxide dispersion and γ′ precipitates, were prepared by mechanical alloying. Hot compression tests were performed in the temperature range of 25–970 °C with the strain rate varying from 0.0001 to 0.01 s^{-1}. The influence of deformation parameters and Y_2O_3 content on the flow behavior and the microstructure of compressive specimens were investigated. It was observed that Co-base ODS alloys had exhibited the homogeneous distribution of ultrafine γ′ precipitates (0.26 μm), nanosized oxide particle (12.5 nm), and small grains (1.1 μm). The enhanced flow stress at low temperatures and high strain rates was attributed to the rapid multiplication of dislocations due to the pining effect of oxide dispersion, γ′ precipitates, and fine grains. The peak stress had decreased with increasing the deformation temperature as well as by decreasing the strain rate. The obvious improvement in flow stress was acquired by increasing the Y_2O_3 contents. Grain boundary sliding and porosity growth had been considered to be the main softening mechanisms during the hot deformation at elevated temperature. Moreover, It was found that the flow softening could be accelerated by decreasing the strain rate. The activation energy had increased with increasing temperature, but decreased with decreasing strain rate.

1. Introduction

Conventional Co-base alloys have been extensively utilized for hot section components of gas turbine engine, such as blade, nozzle, and combustion chamber owing to their superior high-temperature corrosion and oxidation resistance characteristics [1,2]. However, the conventional Co-base alloys lack sufficient high-temperature mechanical properties because of the coarsening or dissolution of carbides at elevated temperature [3]. The high-temperature strength limit of the conventional Co-base alloy would be enhanced by employing the more effective hardening mechanisms of γ′ precipitates and oxide dispersion strengthening (ODS). Oxide particles are highly stable at the temperature beyond 1000 °C, while γ′ strengthening is advantageous in the medium temperature range between 600 and 800 °C [4–6]. The combination of above two strengthening mechanisms has opened the possibility of developing a new-type of Co-base alloy. Therefore, in the present work, we have made an attempt to fabricate the Co-base ODS alloys by the combination of dispersion strengthening for elevated temperature strength and γ′ precipitation hardening for intermediate temperature strength.

To the best of our knowledge, a little information is available about the fabrication and mechanical properties of Co-base ODS alloys produced by the mechanical alloying method. The γ′ precipitate is a relatively new strengthening phase in Co-base alloys, which has been recently discovered in Co–Al–W ternary system by Sato et al. [7–10]. The Co–Al–W base ODS alloys, fabricated by mechanical alloying, have exhibited the complex microstructural evolution during heat treatment originating from the extremely low solubility of Al and W in cobalt matrix at room temperature. Mechanical alloying of this immiscible alloy has induced the formation of supersaturated solid solution, which is a highly nonequilibrium state facilitating the phase separation. However, the decomposition behavior and phase formation mechanism are not yet fully understood. For the oxide dispersion mechanism, oxide particle refinement and the reduction of the distance between the particles are the most important factors contributing to the high-temperature strength of ODS alloys. Our previous study has revealed that the addition of Hf refine the oxide dispersion that in turns results in the amelioration of the high-temperature mechanical properties [11]. Moreover, it has been observed that the microstructural features such as grain size, morphology, size, and the distribution of the oxides and γ′ precipitates determine the high-temperature properties of Co-base ODS alloys. Simultaneously, the thermomechanical processing variables such as deformation temperature and strain rate are found to exert much influence on the deformation behavior and the associated

* Corresponding author. Tel.: +86 10 62332727; fax: +86 10 62334311.
E-mail address: quxh@ustb.edu.cn (X. Qu).

0925-8388/$ – see front matter © 2011 Elsevier B.V. All rights reserved.
doi:10.1016/j.jallcom.2011.08.097

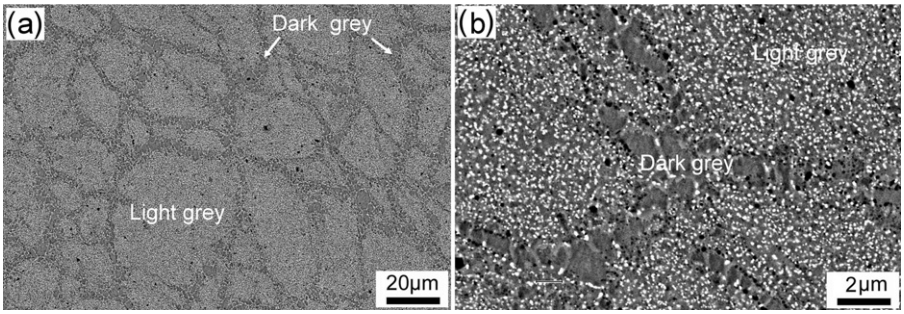

Fig. 1. SEM microstructure of Co-base ODS alloy.

microstructure. Therefore, it is worth investigating and comprehending the influence of oxide refinement and microstructural evolution on the resulting mechanical properties.

In the present paper, a family of Co–Al–W base ODS alloys has been synthesized. Furthermore, the influence of microstructural characteristics and compression parameters on high-temperature hot deformation behavior has been investigated thoroughly. In addition, associated microstructural evolution has been studied to reveal and comprehend the deformation mechanisms. The deduced results can be valuable not only to design the alloying composition, but also to optimize the fabrication processes as well as the better control of microstructure.

2. Experimental procedures

Three kinds of alloys with varied contents of Y_2O_3 were designed and the compositions were given in Table 1. Al and W were γ′ forming elements. Hf was used to refine the oxide particles and thus to increase their number density. Above alloys were mechanical alloyed in a high energy planetary ball mill at a rotation speed of 400–480 rpm with the ball/powder weight ratio of 10:1 in Ar atmosphere for 48 h. The alloys were consolidated by spark plasma sintering (SPS) at 1145 °C with the pressure of 50 MPa. The specimens were solution treated at 1300 °C for 6 h and aged at 900 °C for 24 h.

Phase transformation of the oxides was studied by Siemens D 5000 X-ray diffraction meter using Cu radiation. The polished specimens were etched with a solution of 30%HNO_3 + 70%CH_3OH and the microstructure was characterized by A LEO1450 scanning electron microscope (SEM). The grain size of the specimens was measured by the mean-linear intercept method from SEM images. The TEM specimens were prepared by grinding and ion thinning. Observation of oxide particles was performed using JEM 200 transmission electron microscope (TEM) equipped with energy-dispersive X-ray (EDS). The cylindrical compression specimens of 5 mm in diameter and 10 mm in height were machined from the heat treated 1.5Y alloy. The hot compression tests were conducted using Gleeble-1500 simulator at the deformation temperature from 25 to 970 °C and the strain rate of 0.0001–0.01 s^{-1}. The specimens were soaked for 2 min at the deformation temperature before isothermal compression. The specimens were deformed to the height reductions of 70%. As soon as the deformation was completed, the deformed specimens were immediately quenched by water. Subsequently, the deformed specimens were cut parallel to the deformation axis and the microstructure was observed by SEM.

3. Results and discussion

3.1. Initial microstructure

Size and size distribution of γ′ precipitates and oxide dispersion, as well as the grain size play an important role in determining the high-temperature mechanical properties of Co-base ODS alloy.

Table 1
Chemical composition of the designed alloys (wt.%).

Alloys	Al	W	Y_2O_3	Hf	Co
0.6Y	2.5	13.8	0.6	0.9	Bal.
1Y	2.5	13.8	1.0	1.5	Bal.
1.5Y	2.5	13.8	1.5	2.25	Bal.

3.1.1. γ′ Precipitates

Fig. 1 shows the microstructure of the heat treated specimens before hot deformation. The consolidated alloy has not exhibited any visible pores. It is evident that a high population of fine precipitates is formed. Additionally, light grey area can be clearly differentiated from dark grey area, as depicted in Fig. 1a. It is noted that the light grey area has been surrounded by the dark grey area. It is clearly visible in Fig. 1b that the light grey area constitutes a uniform dispersion of spherical particles with the size of around 0.26 μm, while the dark grey area has exhibited a few or no precipitates. The dark grey area is termed as precipitation free area.

Microstructural formation mechanism of Co-base ODS alloy can be explained as follows: Firstly, mechanical alloying induce the formation of the solid solution supersaturated with Al and W because of the fact that the solubility of Al and W in cobalt matrix is extremely low at room temperature [12,13]. Secondly, the liquid phase is formed during the subsequent sintering that migrates along the prior powder particle under pressure. Since the white precipitates do not contribute to the formation of liquid phase, therefore, their distribution confines to the interior of MA powder particle and constitutes the precipitation free area. It is supposed that dark grey area, shown in Fig. 1a, has been driven off from the liquid phase during sintering. Since the supersaturated solid solution is in a non-equilibrium state, therefore, the spinodal decomposition occurs during aging process leading to the formation of γ′ phase through the following reaction [14]:

$$\gamma + CoAl + Co_3W \rightarrow \gamma' \quad (1)$$

Spinodal decomposition mechanisms have also been previously reported for Co–Al and Co–W systems [15,16]. The microstructural formation mechanism and the factors controlling the size of γ′ precipitates still need to be further investigated.

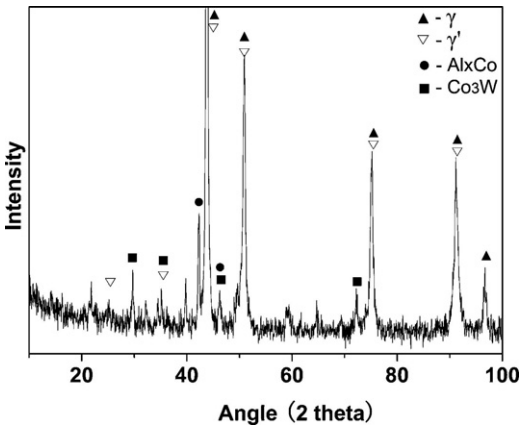

Fig. 2. XRD pattern of Co-base ODS alloy.

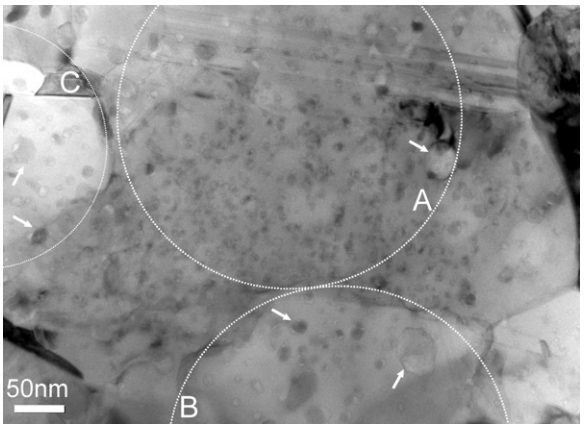

Fig. 3. TEM micrograph of Co-base ODS alloy.

Fig. 2 shows the XRD patterns of heat treated Co-base ODS alloys. The formation of γ′ precipitates is evident. Additionally, the existence of Al_xCo and Co_3W indicates the occurrence of phase decomposition.

3.1.2. Oxide dispersion

Mechanical properties of Co-base ODS alloys at elevated temperatures are critically dependent on the stability of the oxides. On the other hand, the stability of the oxides is closely associated with the interfacial structure of the oxide particles. Fig. 3 displays the TEM image of Co-base ODS alloy. It is evident that the size distribution of oxides is not uniform in the matrix. A high population of nano-sized oxide particles with the size of around 9–15 nm has been detected in the area marked by A. However, the oxide particles, slightly poor in density in the, area are marked by B and C. The particles up to 40 nm can be found in the areas marked by the arrows shown in Fig. 3. The non-uniform distribution of oxide particles is related to the structure of Co-base ODS alloys and it needs to be further investigated [2]. The ultrafine oxides with partially coherent interface are formed by the size refinement effect of Hf, while the larger oxides are ascribed to the addition of Al and the participation of liquid phase during sintering favoring the growth of oxides. The average size of oxide particles is determined to be 12.5 nm.

Fig. 4a presents the high-resolution transmission electron microscopy (HRTEM) image of a nanosized oxide particle. The oxides, visible in Fig. 4a, are spherical and its average diameter is less than 10 nm. The plane distance measured are 2.74 Å and 2.76 Å, which corresponds to (1 1 0) and (1 1 1) planes of $Y_2Hf_2O_7$ oxides, respectively. Thus, the chemical form of oxide particle transforms from Y_2O_3 to $Y_2Hf_2O_7$. The lattice continuity between the oxides and the surrounding matrix is clearly observed. Additionally, the observation of facet and ledge interface is an indication of the formation of partial coherent interface [17]. The reduced interfacial energy is beneficial to enhance the stability of oxides. The EDS analysis, shown in Fig. 4b, reveals that the ultrafine oxides are rich in Hf, indicating that the formation of Y–Hf–O oxides is responsible for the refinement of oxide particles.

3.1.3. Grain structure

Fig. 5 shows the grain structure of the heat treated Co-base ODS alloy. The grain size is as small as several micrometers, which is attributed to the pinning of oxide dispersion and γ′ precipitates. It is evident that grain size is not uniform. Clearly, there are two visible regions with different grain size. One area is comprised of relatively large grain size of 1–4 μm, as marked by L in Fig. 5a; the other one consists of fine grains with dimensions of about 0.25–1 μm, as marked by S in Fig. 5a. This structure is identified as a bimodal grain size distribution, which is similar to the grain structure found in ODS steels [18–20]. It has also been observed in Fig. 5b that the ultrafine grains are surrounded by the relatively large grains. Additionally, the large grains are within the precipitation free area, indicating that the pining effect of dispersion is larger in precipitation free area than that in the interior region with small grains.

Fig. 6 illustrates the grain size distribution of Co-base ODS alloy evaluated from Fig. 5. It is further confirmed that the grain size is in a micrometer range. The distribution exhibits the feature of bimodal grain size distribution. Two peaks in the size range of 0.5–0.75 μm and 1.25–1.5 μm are detected. The analysis of grain size distribution reveals that the average grain size is about 1.1 μm.

3.2. Deformation parameters dependence of flow behavior

3.2.1. True stress–true strain curves

The true stress–true strain curves of Co-base ODS alloys, compressed at various temperatures from 25 °C to 950 °C under strain rate of 0.0001–0.01 s^{-1} are shown in Fig. 7. The measured flow stress of Co-base ODS alloys shows a strong dependence on deformation temperature and strain rates. Fig. 7a reveals the occurrence of strain hardening at room temperature. It is evident that the flow stress increases monotonously with the increase in strain until fracture. No major variation in peak stress has been observed at room temperature. The peak stress values under the strain rates of 0.01 s^{-1} and 0.001–0.0001 s^{-1} are 989 MPa, 1050 MPa, and 1080 MPa, respectively. The pronounced work hardening behavior is associated with a rapid multiplication of dislocations. High density of γ′ precipitates and nanosized oxide dispersion are the

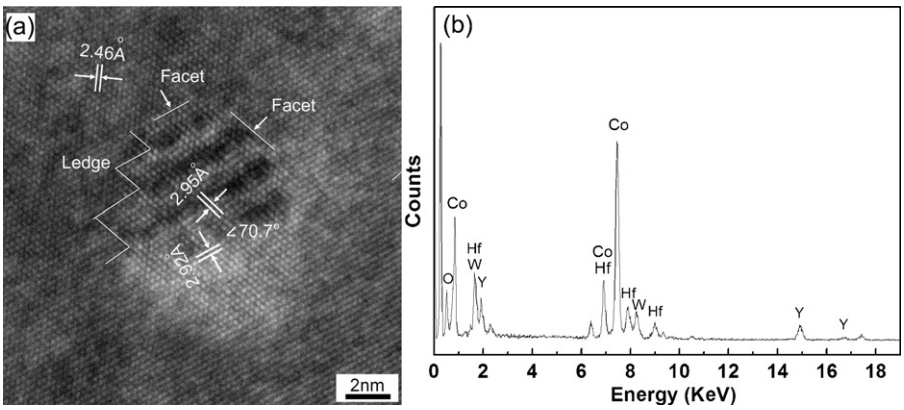

Fig. 4. HRTEM image of ultrafine oxide (a) and the EDS results (b).

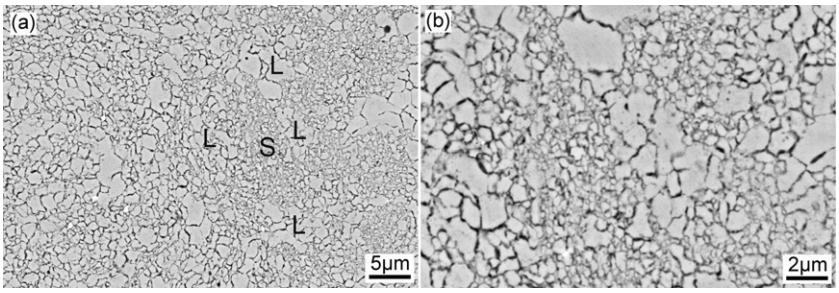

Fig. 5. Grain structure of Co-base ODS alloy.

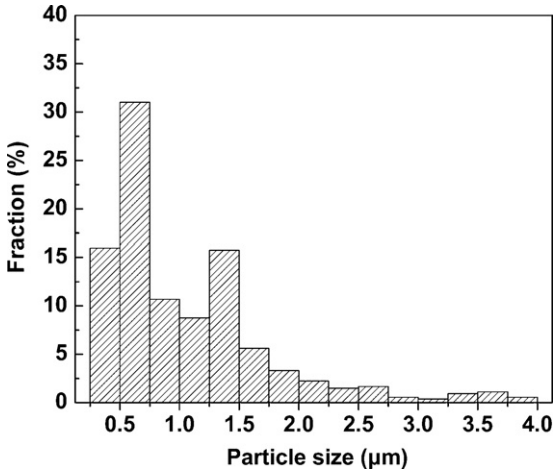

Fig. 6. Grain size distribution of Co-base ODS alloy.

major source of the high peak stress at room temperature. However, this increase in strength is accompanied by a low uniform elongation. The specimens tested at higher temperature exhibit larger fracture elongation compared with the specimens tested at room temperature. Fig. 7b–d shows the stress–strain curves of Co-base ODS alloys deformed under the strain rates of 0.01 s^{-1} and 0.001–0.0001 s^{-1}. As the strain increases, the stress increases monotonously and reached a steady state, indicating that work hardening is insignificant. The flow stress decreases with increasing deformation temperature at a given strain rate. This phenomenon may be attributed to the lower atomic critical shear stress resulting from the enhanced thermal activation at higher temperature. The high temperature facilitates the softening during deformation. As the temperature reaches beyond 800 °C, a pronounced decrease in flow stress becomes evident. Moreover, this decrease in strength is generally attended by an increase in the ductility. Lowering the strain rate also renders the drop in flow stress at a given testing temperature. Another feature of the curves is the lack of peak stress which is usually identified by a large drop in the stress value after attaining a peak stress. It indicates that dynamic recovering is not the dominant softening mechanism. However, the flow softening due to dynamic recovering can be compensated by the strengthening of γ′ precipitates and oxide dispersion. At higher deformation temperature (>800 °C), work softening becomes more significant. The grain boundary sliding and the formation of porosity are considered as the high-temperature softening mechanisms and can be further verified by further analysis of the microstructure in the latter section. The fluctuation of the flow curves tested at the strain rate of 0.0001 s^{-1} may be caused by porosity formation and growth.

Fig. 8 depicts the variation of peak stress as a function of temperature at different strain rates. From this plot, it is found that at a fixed strain rate, the peak stress decreases with increasing temperature up to 970 °C. Furthermore, the decreasing rate is lager in the temperature range of 600–800 °C than that in the range of 800–970 °C. At a given temperature, peak stress diminishes with decreasing strain rate and moreover, the effect of strain rate is

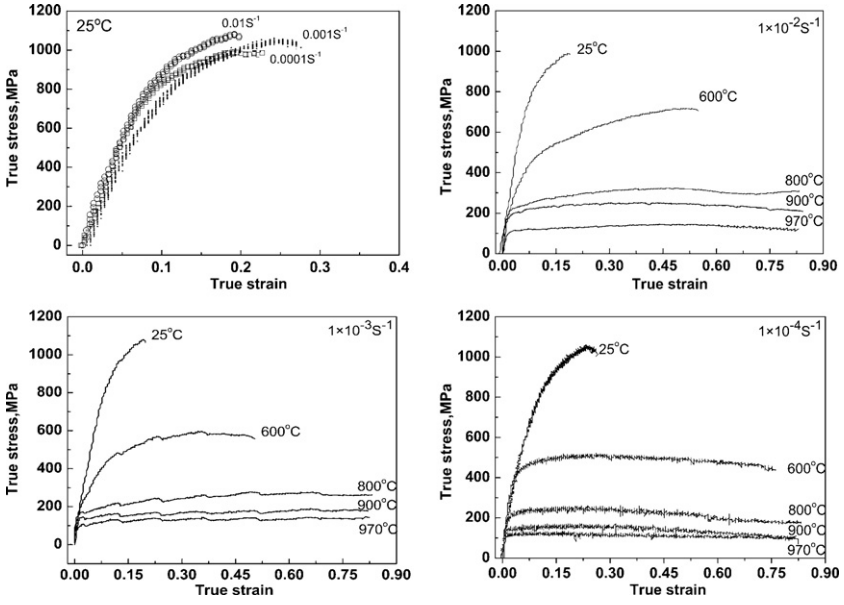

Fig. 7. True stress–strain curves of Co-base ODS alloys at various deformation conditions: (a) 25 °C, (b) 1×10^{-2} s^{-1}; (c) 1×10^{-3} s^{-1} and (d) 1×10^{-1} s^{-1}.

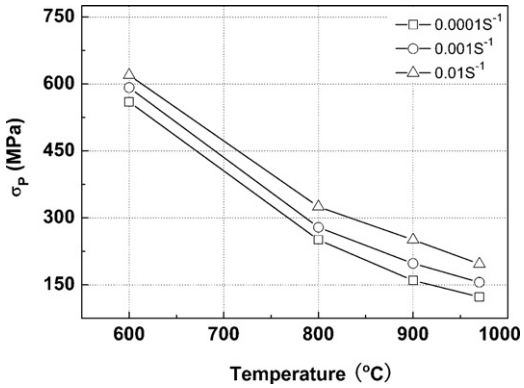

Fig. 8. Evolution of peak stress as a function of temperature at different strain rates.

significant at lower strain rate. The relatively low peak stress under high temperature and lower strain rate is associated with the fine-grained structure of Co-base ODS alloys.

3.2.2. Kinetics of hot deformation

During hot deformation, the dependence of flow stress on the deformation temperature and strain rate can be expressed as [21]:

$$Z = \dot{\varepsilon} \exp\left(\frac{Q}{RT}\right) = f_1(\sigma) = A\sigma^{n_1} \quad (2)$$

$$Z = f_2(\sigma) = B \exp(\beta\sigma) \quad (3)$$

where Z is the Zener–Hollomon parameter, $\dot{\varepsilon}$ is the strain rate (s^{-1}), Q is activation energy of deformation (kJ/mol^{-1}), R is the gas constant, T is absolute temperature (K) and A, B, n_1 and β are material constants, σ is the stress often replaced by the peak stress σ_p (MPa). The power law (Eq. (2)) and the exponent-type equation (Eq. (3)) break at a high stress and at a low stress, respectively. Eq. (4) is another more general constitutive equation suitable for stresses over a wide range [22]:

$$Z = f(\sigma) = A[\sinh(\alpha\sigma)]^n \quad (4)$$

where A and α are the material constants, n is the stress exponent. α, β and n are related by the equation:

$$\alpha = \frac{\beta}{n} \approx \frac{\beta}{n_1} \quad (5)$$

α can be calculated by the following equation using the data shown in Fig. 9.

$$\alpha = \frac{(\alpha \ln \dot{\varepsilon}/\alpha\sigma_P)|_T}{(\alpha \ln \dot{\varepsilon}/\alpha \ln \sigma_P)|_T} \quad (6)$$

From Eq. (4), the activation energy at the peak stress of the flow curves can be derived as [23]:

$$Q = R\frac{\partial \ln \dot{\varepsilon}}{\partial \ln[\sinh(\alpha\sigma_p)]}|_T \frac{\partial \ln[\sinh(\alpha\sigma_p)]}{\partial(1/T)}|_{\dot{\varepsilon}} \quad (7)$$

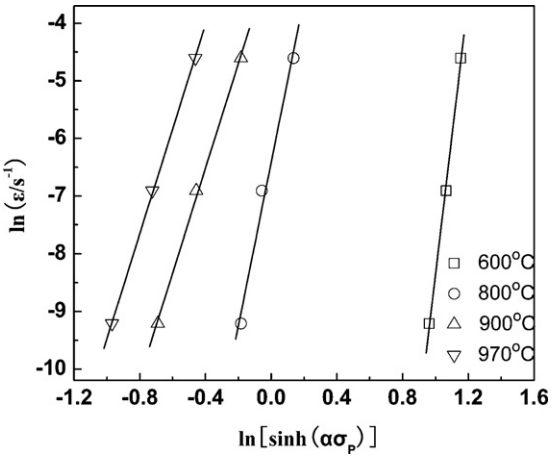

Fig. 10. Correlation of ln[sinh($\alpha\sigma_p$)] to ln $\dot{\varepsilon}$ under the temperature of 600–970 °C.

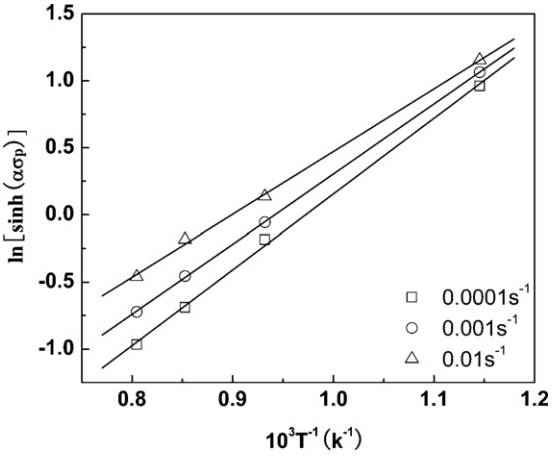

Fig. 11. Correlation of ln[sinh($\alpha\sigma_p$)] to $1/T$ at the strain rates of 0.01 s^{-1}, 0.001 s^{-1} and 0.0001 s^{-1}.

As shown in Figs. 10 and 11, by estimating the slopes of the graphs ln $\dot{\varepsilon}$ *vs.* ln[sinh($\alpha\sigma$)] at various temperatures, and ln[sinh($\alpha\sigma$)] *vs.* ln(1000/T) at various strain rates, the Q values calculated at each stain rate and temperature were listed in Table 2.

Table 2 clearly depicts that the activation energy is much higher under the conditions of higher strain rate and lower temperature. At a fixed temperature, Q value decreases with increasing temperature. At a given temperature, Q value decreases with decreasing strain rate. Q value is estimated to be 1103 kJ/mol at the strain rate of 0.01 s^{-1} and at the temperature of 600 °C. At the strain rate of 0.0001 s^{-1} and temperature 900 °C, Q value diminishes to 346 kJ/mol, which is very close to the activation energy for self

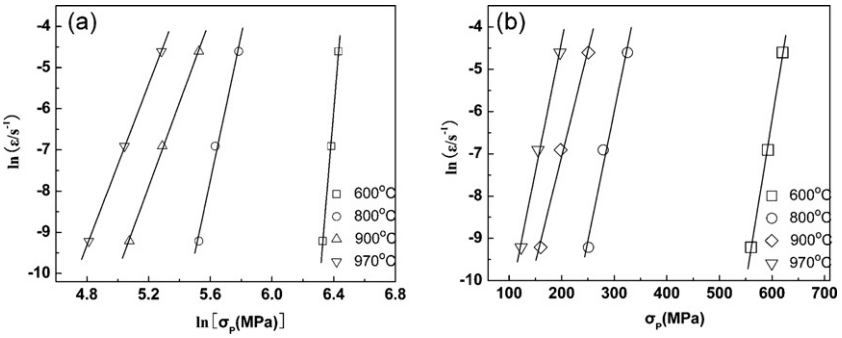

Fig. 9. Variations in peak stress of the as-cast alloy as a function of strain rate: (a) ln- and (b) ln–ln scale at different temperatures.

Table 2
Apparent activation energy of Co-base ODS alloy.

Temperature	Q (kJ/mol)		
	0.01 s^{-1}	0.001 s^{-1}	0.0001 s^{-1}
600 °C	1103	1020	913
800 °C	653	604	541
900 °C	418	387	346
970 °C	418	387	345

diffusion of cobalt (270 kJ/mol) [24]. The change in activation energy implies the change in deformation mechanisms. At lower temperature and higher strain rate, oxide dispersion, γ′ precipitates, and fine grains are effective to drag the motion of dislocation during the deformation process resulting in a high Q value. However, the occurrence of grain boundary sliding at elevated temperature decreases the dislocation density culminating in the deterioration of activation energy.

3.3. Y_2O_3 content dependence of flow behavior

Fig. 12 illustrates the true stress–true strain curves of Co-base ODS alloys with varied Y_2O_3 content at the strain rate of 0.01 s^{-1} and at the temperature of 900 °C. It is evident that both deformation temperature and Y_2O_3 content have considerable influence on the flow stress. Obvious improvement in the flow stress has been acquired with increasing Y_2O_3 content. The peak flow stress of 0.6Y, 1.0Y and 1.5Y alloys is 150 MPa, 207 MPa and 251 MPa, respectively.

The resistance of obstacles to dislocation motion deteriorates the flow stress of the alloys at high temperature. The dislocation motion in ODS alloys is hampered by the strong obstacles. The mechanisms that dominate the interaction between dislocation and dispersions are different at various temperatures. In order to comprehend the deformation mechanisms responsible for the flow behavior of the alloys with varied content of Y_2O_3, the relationship between the particle dispersion and the strength increment has been examined. The contribution to strength from dispersion strengthening is estimated by the threshold stress, which is a well known quantitative value determining the effect of oxide dispersion. Threshold stress can be calculated using the size distribution by the following equation [25,26]:

$$\sigma\text{th} = A\frac{M}{2\pi}\frac{Gb}{\lambda}\left(\ln s\frac{\bar{D}}{r_0} + B\right) \quad (8)$$

where A and B are constants depending on the strengthening mechanisms and the characteristics of dislocation, which are taken

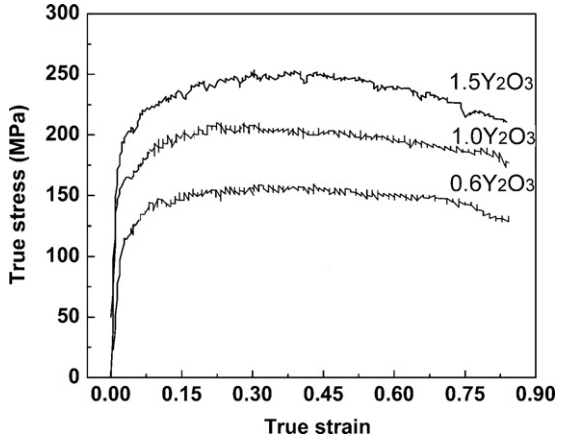

Fig. 12. True stress–strain curves of the alloys with varied content of Y_2O_3 tested at 900 °C and the strain rate of 0.01 s^{-1}.

Table 3
Calculated threshold stress of the alloys with varied Y_2O_3 contents at room temperature and 900 °C.

Temperature	Strengthening mechanism	Dispersion strength (MPa)		
		0.6Y	1.0Y	1.5Y
Room temperature	Orowan mechanism	364	479	598
900 °C	Srolovitz mechanism	221	290	362

as 1.06 and 0.65, respectively. G is the shear modulus, b is the Burgers vector, r_0 is the inner cut-off radius of dislocation core, M is the Taylor factor (3.0), r_0 is usually taken as b–3b. $\bar{D}$ is calculated from particle radius and volume fraction (f). The oxide particle size distribution is assumed to be the same and the volume fraction is the only variant. The volume fractions (f) of dispersion, calculated by using the rule of mixture, for 0.6Y, 1Y and 1.5Y alloys are estimated to be 1.06%, 1.76%, and 2.64%, respectively. The shear modulus (G) is taken as 75 GPa at room temperature and 53.7 GPa at the temperature of 900 °C. Table 3 lists the dispersion strength of the alloys, calculated from Eq. (8), by using the following values: $M = 2$, $b = 0.248$ nm, $r_0 = b$ and 3b. Table 3 clearly reveals that the threshold stress is much higher at room temperature than that under 900 °C. A threshold stress for oxide dispersion strengthening has been estimated to be 598 MPa at 25 °C and 362 MPa at 900 °C for 1.5Y alloy.

At room temperature, the measured flow stress of the alloy is around 1050 MPa (Fig. 7a), which is higher than the predicted threshold stress (598 MPa). Besides oxide dispersion, γ′ precipitates and fine grains also contribute to the increase in flow stress, leading to high flow stress at room temperature. In the case of 900 °C, the measured flow stress values of 0.6Y, 1Y, and 1.5Y alloys are significantly lower than the threshold stress predicted by Eq. (8), indicating that the deformation mechanism is not controlled by dislocation–particle interaction. Owing to the fact that low strain and high temperature considerably debilitate the grain boundaries, the low flow stress of the fine grained Co-base ODS alloys arise mainly from the accelerated deformation by grain boundary sliding. In addition, cavity nucleation and growth greatly reduce the flow stress. A removal of the precipitation free area and the coarsening of grain size can be effective ways to further ameliorate the high temperature strength of Co-base ODS alloy.

3.4. Deformation microstructure

In order to correlate the stress–strain behavior with microstructural evolution and to reveal the deformation mechanism of Co-base ODS alloy, the microstructural variations of the deformed specimens are examined. Fig. 13 shows the microstructures of Co-base ODS alloys deformed at various compression parameters. It can be seen from Fig. 13a that at relatively high strain rate of 0.01 s^{-1}, the small amount of porosity has been observed. However, for the specimens tested at the strain rate of 0.001 s^{-1}, the amount of porosity increases and the presence of a few large pores is an indicative of coalescence of microvoids (Fig. 13b). For comparison, testing at the strain rate of 0.0001 s^{-1} leads to the formation of a lot of microvoids and microcracks, as marked in Fig. 13c. This phenomenon is associated with extensive porosity and subcritical crack growth. As far as the morphology of precipitates is concerned, a few relatively large plate-like precipitates have been observed, which is the outcome of the destabilization of the precipitates during deformation. However, the stability of the fine precipitates needs to be further investigated.

The formation mechanism of porosity during hot deformation can be attributed to the following reasons. First, the fine grained Co-base ODS alloys are strengthened by a high population of γ′ precipitates and oxide dispersion, as well as a high density of

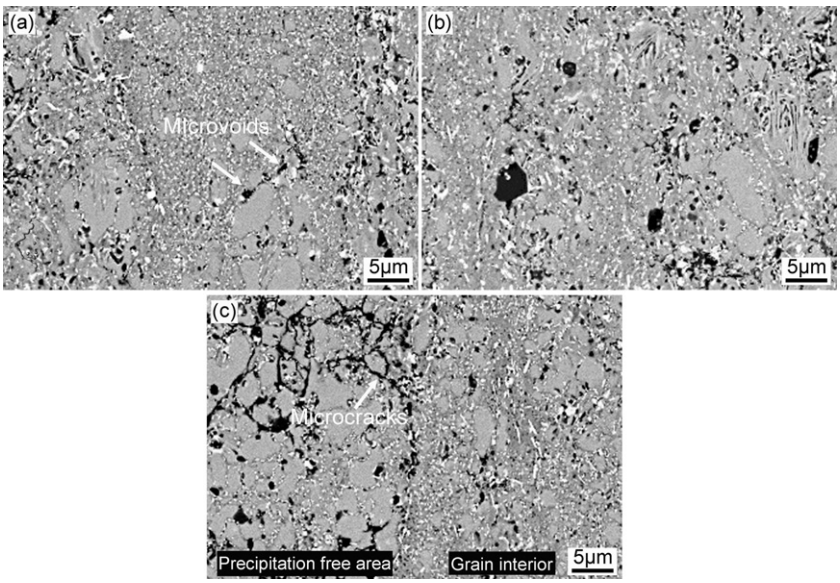

Fig. 13. Microstructure of the deformed Co-base ODS alloys tested at 970 °C with the strain rates of: (a) 0.01 s^{-1}, (b) 0.001 s^{-1} and (c) 0.0001 s^{-1}.

grain boundaries. During hot deformation, grain boundaries were weaker regions compared to grain interior, while grain interiors have high resistance to deformation at high temperature. Grain interiors have no sufficient plasticity to accommodate the deformation of grain boundary sliding, resulting in the rapid formation of extensive microvoids or intergranular cracks. The fine grains provide convenient paths for mass diffusion, which is conducive to the grain boundary sliding [27]. The higher temperature and the lower strain rate accelerate the nucleation and growth of porosity. The lower strain rate supplements the sufficient time for cavity coalescence resulting in stable cavity growth that ultimately leads to the formation of many large pores and considerable softening. This result coincides with the earlier observation about the formation of porosity in the fine-grained ODS steels [28]. Additionally, the presence of precipitation free area and the non-uniform distribution of oxide dispersion render the stress accumulation that preferably originates the grain boundary sliding and fracture [29]. It is fact that porosity and microcracks accumulate more preferably in precipitation free area than interior grains. The stress concentration can be released by self-diffusion. The higher temperature and the lower strain rates result in enhanced atomic diffusion and lower dislocation densities, leading to the faster grain boundary mobility and hence the generation of more porosity. The low flow stress is certainly related to the presence of porosity. Moreover, oxidation may accelerate the failure of Co-base ODS alloys due to the aggregation of oxidation under high temperature and low strain rate.

Fig. 14 shows the SEM fracture surface of three specimens tested under three typical deformation conditions. The specimens, deformed at high strain rate (0.01 s^{-1}) and low temperature (25 °C), exhibit the typical cleavage fracture mode with the presence of few porosity (Fig. 14a). It is believed that the excessive strengthening of γ' phase and oxides tend to induce cleavage fracture and low ductility, which is detrimental to the plastic deformability. These results explain far its high strength and low ductility. On the contrary, the specimens, deformed at the lowest strain rate (0.0001 s^{-1}) and the

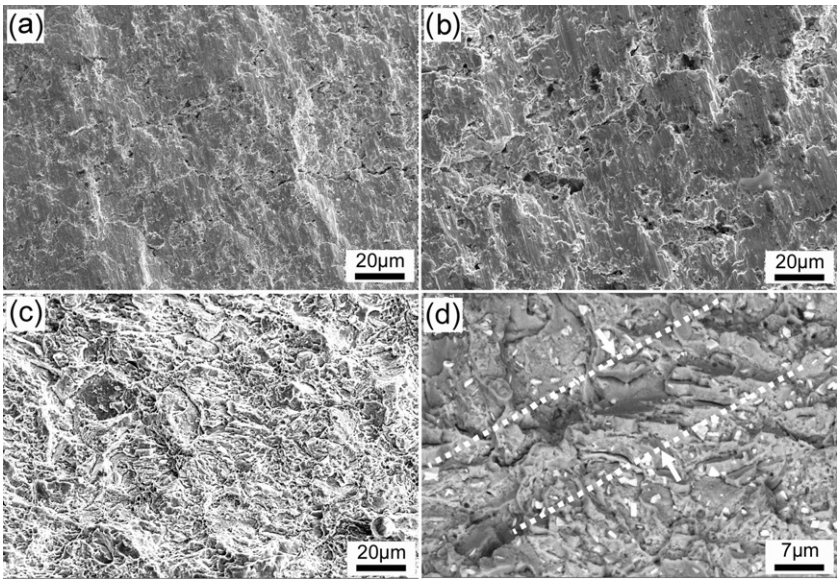

Fig. 14. Fractural morphology of the samples deformed at the conditions of: (a) 0.01 s^{-1}, 25 °C; (b) 0.0001 s^{-1}, 970 °C; and (c and d) 0.001 s^{-1}, 900 °C.

highest temperature (970 °C), presents a large amount of porosity owing to the grain boundary sliding (Fig. 14b), leading to the cleavage fracture mode. It is seen in Fig. 14c that the fracture surface of the specimens, deformed at intermediate strain rate ($0.001\ s^{-1}$) and temperature (800 °C), exhibits the transgranular dimpled feature, which is indicative of a ductile fracture mode. Fig. 14d shows the backscattered electron images of the fractured surface. It is worth noting that the feature of plastic deformation is more obvious in the precipitation free area, suggesting that precipitation free area is relatively weak region.

4. Conclusions

The hot deformation testes and microstructure characterization have been performed on Co-base ODS alloys. The following conclusions can be drawn from the results of this investigation:

(1) Co-base ODS alloys are characterized by uniform γ' precipitates with the size of 0.5 μm, nanosized (average size of 15 nm) oxide dispersion with partially coherent interface, and fine (average grain size of 0.5 μm) grain size.
(2) The pronounced work hardening has been observed at room temperature due to the pining effect of oxide dispersion, γ' precipitates, and fine grains. The peak stress decreases with increasing deformation temperature and decreasing strain rate. The obvious amelioration of flow stress is acquired by enhancing the Y_2O_3 contents.
(3) The activation energy increases with increasing temperature, but decreases with decreasing strain rate.
(4) Grain boundary sliding and porosity growth at higher temperature and lower strain rate are considered to be responsible for the low flow stress. Flow softening can be accelerated by increasing the temperature as well as by decreasing the strain rate.

Acknowledgement

The research was financially supported by National Nature Science Foundation of China (51104007) and National Postdoctoral Foundation of China (20100480198, 1104053).

References

[1] C.F. Tang, F. Pan, X.H. Qu, C.C. Jia, B.H. Duan, J. Mater. Process. Technol. 204 (2008) 111–116.
[2] K. Takezawa, S. Ukai, S. Hayashi, Adv. Mater. Res. 239–242 (2011) 864–867.
[3] S.H. Zangeneh, H. Farhangi, Mater. Des. 31 (2010) 3504–3511.
[4] M. Nganbe, M. Heilmaier, Mater. Sci. Eng. A 387–389 (2004) 609–612.
[5] L.J. Park, H.J. Ryu, S.H. Hong, Y.G. Kim, Adv. Perform. Mater. 5 (1998) 279–290.
[6] M. Nganbe, M. Heilmaier, Int. J. Plast. 25 (2009) 822–837.
[7] J. Sato, T. Omori, K. Oikawa, I. Ohnuma, R. Karinuma, K. Ishida, Science 312 (2006) 90.
[8] K. Shinagawa, T. Omori, K. Oikawa, R. Kainuma, Scripta Mater. 61 (2009) 612–615.
[9] A. Suzuki, J.M. Pollock, Acta Mater. 56 (2008) 1288–1297.
[10] K. Shinagawa, T. Omori, J. Sato, K. Oikawa, I. Ohnuma, Mater. Trans. 49 (2008) 1474–1479.
[11] L. Zhang, S. Ukai, T. Hoshino, S. Hayashi, X.H. Qu, Acta Mater. 57 (2009) 3671–3682.
[12] A.M. Mebed, M.I. Abd-Elrahmany, Phase Transitions 82 (2009) 587–598.
[13] M. Zhu, X.Z. Che, Z.X. Li, J. Mater. Sci. 33 (1998) 5873–5881.
[14] S. Kobayashi, Y. Tsukamoto, T. Takasugi, H. Chinen, Intermetallics 17 (2009) 1085–1089.
[15] G. Östberg, B. Jansson, H.O. Andrén, Scripta Mater. 54 (2006) 595–598.
[16] K. Niitsu, T. Omori, M. Nagasako, K. Oikawa, J. Alloys Compd. 509 (2011) 2697–2702.
[17] M. Klimiankou, R. Lindau, A. Moslang, J. Cryst. Growth 249 (2003) 381–387.
[18] C.C. Eiselt, M. Klimenkov, R. Lindau, A. Mölang, H.R.Z. Sandim, A.F. Padilha, D. Raabe, J. Nucl. Mater. 385 (2009) 231–235.
[19] P. Miao, G.R. Odette, T. Yamato, M. Alinger, D. Hoelzer, D. Gragg, J. Nucl. Mater. 367–370 (2007) 208–212.
[20] Z. Oksiuta, N. Baluc, J. Nucl. Mater. 374 (2008) 178–184.
[21] F.W. Kang, J.F. Sun, G.Q. Zhang, Z. Li, J. Mater. Sci. Technol. 25 (2009) 373–378.
[22] C.M. Sellars, W.J. Tegart, Membr. Sci. Rev. Met. 63 (1966) 731–746.
[23] F.W. Kangab, G.Q. Zhangc, J.F. Suna, Z. Lic, J. Shena, J. Mater. Process. Technol. 204 (2008) 147–151.
[24] B. Paul, R. Kapoor, J.K. Chakravartty, A.C. Bidaye, I.G. Sharma, A.K. Suri, Scripta Mater. 60 (2009) 104–107.
[25] H. Sakasegawa, L. Chaffron, F. Legendre, J. Nucl. Mater. 386–388 (2009) 511.
[26] S. Ukai, S. Ohtsuka, T. Kaito, H. Sakasegawa, Mater. Sci. Eng. A 510–511 (2009) 115–120.
[27] S. Takaki, K. Kawasaki, Y. Kimura, J. Mater. Process. Technol. 117 (2001) 359–363.
[28] T.C. Toterneier, T.M. Lillo, J.A. Simpson, Metall. Mater. Trans. A 36 (2005) 2552–2555.
[29] S. Ukai, S. Ohtsuka, T. Kaito, H. Sakasegawa, N. Chikata, S. Hayashi, S. Ohnuki, Mater. Sci. Eng. A 510–511 (2009) 115–120.